Quasigeostrophic models of convection in rotating sperical shells.

J. Aubert, N. Gillet, Philippe Cardin

Geochemistry Geophysics Geosystems G3
AN ELECTRONIC JOURNAL OF THE EARTH SCIENCES
Published by AGU and the Geochemical Society

Article
Volume 4, Number 7
3 July 2003
1052, doi:10.1029/2002GC000456
ISSN: 1525-2027

Quasigeostrophic models of convection in rotating spherical shells

Julien Aubert
Institut for Geophysics of the University of Goettingen, Herzberger Landstrasse 180, Goettingen 37075, Germany (jaubert@gwdg.de)

Nicolas Gillet and Philippe Cardin
Laboratoire de Géophysique Interne et Tectonophysique, Observatoire de Grenoble, B.P. 53, 38041 Grenoble, France (ngillet@ujf-grenoble.fr; pcardin@ujf-grenoble.fr)

[1] The use of a quasigeostrophic, two-dimensional approximation in the problem of convection in a rapidly rotating spherical shell has been limited so far to investigations of the qualitative behavior of the solution. In this study, we build a quasigeostrophic model that agrees quantitatively with full three-dimensional solutions of the onset of convection in the case of differential heating. Reducing the dimensionality of the problem also permits the simulation of finite amplitude regimes of convection, up to quasigeostrophic turbulence. The nonlinear behavior of the system is studied in detail and compared to ultrasonic Doppler velocimetry measurements performed in a convecting, rapidly rotating spherical shell filled with water and liquid gallium. The results are quantitatively satisfactory and open the way to less computer-demanding, and still accurate, simulations of the geodynamo.

Components: 8168 words, 13 figures, 1 table, 2 dynamic content.

Keywords: Geodynamo; convection; quasigeostrophic numerical models.

Index Terms: 1507 Geomagnetism and Paleomagnetism: Core processes (8115); 1510 Geomagnetism and Paleomagnetism: Dynamo theories.

Received 17 October 2002; **Revised** 19 February 2003; **Accepted** 19 March 2003; **Published** 3 July 2003.

Aubert, J., N. Gillet, and P. Cardin, Quasigeostrophic models of convection in rotating spherical shells, *Geochem. Geophys. Geosyst.*, *4*(7), 1052, doi:10.1029/2002GC000456, 2003.

1. Introduction

[2] The problem of convection in rapidly rotating spherical shells is central to several issues in the physics of planetary interiors. Recently [*Manneville and Olson*, 1996; *Christensen*, 2001] the subject has gained interest as a possible deep source for large scale zonal circulations such as observed on Jupiter and gaseous planets. Historically it was first considered as a model for the driving power source of the self-sustained dynamos in planetary cores. This process is thought to operate in a parameter range which is well beyond what can be simulated numerically and experimentally. The dominance of the Coriolis force, which is measured by a low Ekman number $E = \nu/\Omega D^2$, where ν is the fluid kinematic viscosity, Ω is the rotation rate and D the shell thickness, implies the existence of thin boundary layers. In liquid metals, where the magnetic diffusivity is much larger than the viscosity, the fluid has to be strongly forced to overcome the threshold for dynamo action, and

therefore a fine-scale turbulence is probably present [*Aubert et al.*, 2001]. Under these circumstances, three-dimensional modeling of such flows is extremely computer-demanding. As a result, despite remarkable advances in the theoretical understanding of the convection onset [*Busse*, 1970; *Jones et al.*, 2000], few studies have addressed the problem of finite-amplitude convection in rapidly rotating spherical shells. Three-dimensional numerical studies (recently [*Christensen*, 2002]) are limited to fairly high Ekman numbers, larger than 10^{-5}. Experiments, as pioneered by [*Busse and Carrigan*, 1976] (recently [*Sumita and Olson*, 2000; *Aubert et al.*, 2001]) achieve lower Ekman numbers, but allow only an incomplete imaging of the flow structure through temperature or velocity measurements. (for a review see [*Nataf*, 2003]).

[3] However, the columnar structure observed at the onset of convection [*Busse*, 1970; *Carrigan and Busse*, 1983] is maintained when going in the finite-amplitude regime [*Cardin and Olson*, 1992] provided the Rossby number is small ($Ro = U/\Omega D$, where U is a typical velocity in the fluid). Fully three-dimensional numerical computations [*Christensen*, 2002] agree with this observation up to a Rossby number of 10^{-2}, when quasigeostrophy does not hold anymore. It has therefore been inferred [*Cardin and Olson*, 1994] that numerical solutions of the equations integrated along the direction (say $\mathbf{e}_z$) of the rotation axis could at least qualitatively model the flow in low Rossby number situations. The resulting quasigeostrophic model describes the time evolution of the z-component of vorticity, and of the z-averaged temperature field, in the equatorial plane. A geostrophic zonal flow is excited through Reynolds stresses. In their study, Cardin and Olson only included bulk viscosity friction to limit the zonal flow. However, [*Aubert et al.*, 2001] pointed out that in their liquid gallium experiments, viscous friction in the interior of the fluid could not explain the magnitude of the observed zonal flow, and that the correct limiting factor was Ekman friction on the outer boundary. The purpose of this paper is to build a quasigeostrophic model that successfully reproduces as many observations of previous experiments as possible. To that extent, the inclusion of Ekman friction leads to a behavior of the system which differs significantly from the numerical work of [*Cardin and Olson*, 1994].

[4] In the next section of this paper we establish quasigeostrophic equations for rotating convection. Section 3 contains the linear study of the model in the case of differential heating. Section 4 presents the dynamic and thermal aspects of nonlinear calculations. In section 5 the model is compared with previously published experiments. The relevance and implications of the results is then discussed in section 6.

2. Equations and Numerical Method

[5] We study thermal convection of a Boussinesq fluid in a rotating spherical shell contained between two concentric spheres of radius r_i and r_e. Figure 1 gives a detailed view of the geometry and some of the notations. The whole approach aims at describing motion outside the tangent cylinder. A cylindrical reference frame ($\mathbf{e}_s$, $\mathbf{e}_\theta$, $\mathbf{e}_z$), the rotation vector $\mathbf{\Omega}$ being parallel to $\mathbf{e}_z$, is adopted, and gravity $g = \Omega^2 s$ is assumed to grow linearly with the cylindrical radius s, a situation which is suitable for description of centrifugal gravity experiments, and also for radial gravity in a self-gravitating body, since in rapidly rotating systems forces parallel to the rotation axis have little dynamical importance, a point which has been verified for thermal convection by [*Glatzmaier and Olson*, 1993].

[6] With the shell thickness $D = r_e - r_i$ as length scale, the viscous diffusion time D^2/ν as time scale and $\Delta T\nu/\kappa$, where κ is the thermal diffusivity, as temperature scale, the equations governing the velocity $\mathbf{u}$, temperature T and pressure Π are:

$$\frac{\partial \mathbf{u}}{\partial t} + (\mathbf{u}\cdot\nabla)\mathbf{u} + 2E^{-1}\mathbf{e}_z \times \mathbf{u} = -E^{-1}\nabla\Pi - Ras\mathbf{e}_s T + \nabla^2\mathbf{u} \tag{1}$$

$$\frac{\partial T}{\partial t} + (\mathbf{u}\cdot\nabla)T = P^{-1}\nabla^2 T \tag{2}$$

$$\nabla\cdot\mathbf{u} = 0. \tag{3}$$

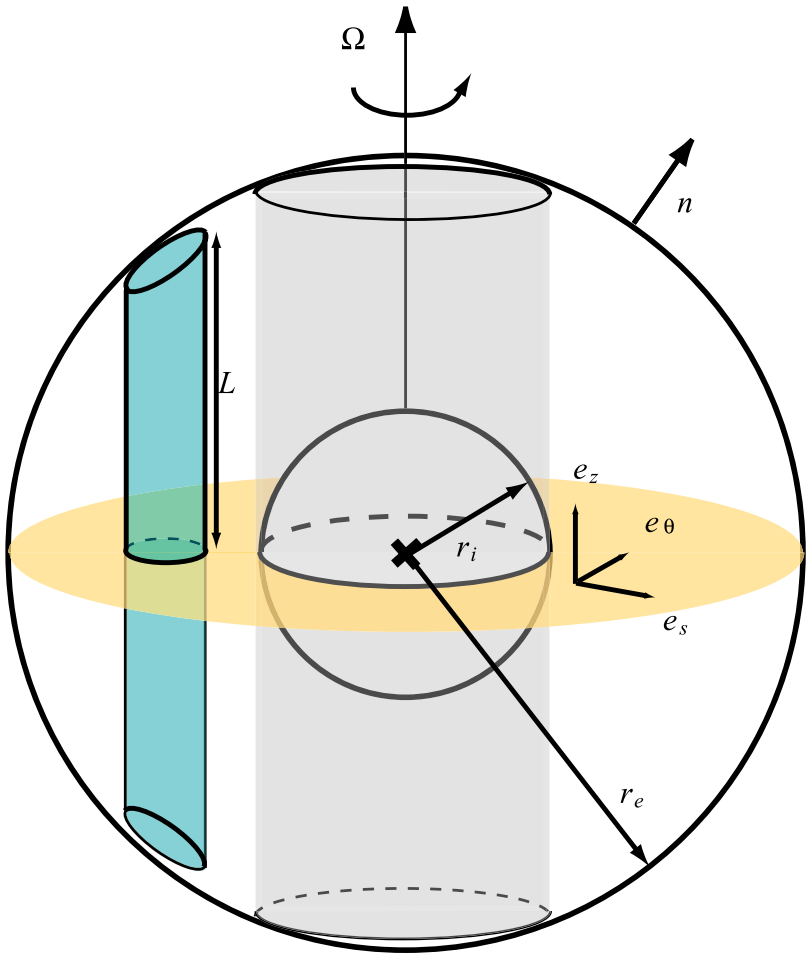

Figure 1. Sketch of the problem geometry. The quasigeostrophic approach solves the fluid motion equations only in the equatorial plane (in yellow), assuming a columnar structure (in blue) for convection cells. Motion within the tangent cylinder (in grey) is not described by the present model. A cylindrical reference frame ($\mathbf{e}_s$, $\mathbf{e}_\theta$, $\mathbf{e}_z$) is chosen.

[7] The velocity field $\mathbf{u}$ satisfies no-slip boundary conditions at the boundaries $r = r_i$ and $r = r_e$, which are maintained at constant temperatures T_i and T_e. Since the gravity is centrifugal, the unstable gradient is $\Delta T = T_e - T_i > 0$. Ra is the Rayleigh number,

$$Ra = \frac{\alpha \Delta T \Omega^2 D^4}{\kappa \nu}, \tag{4}$$

where α is thermal expansivity. $P = \nu/\kappa$ is the fluid Prandtl number. We wish to describe slow motion, i.e., motion with a small frequency when compared to the rotation rate, as is the case for thermal Rossby waves [*Busse*, 1970]. When looking at finite amplitude convection, we also make the assumption of low Rossby number. For such motion, the dominant terms in equation (1) lead to the geostrophic balance:

$$2\mathbf{e}_z \times \mathbf{u} = -\nabla \Pi. \tag{5}$$

Taking the curl of equation (5) yields the Proudman-Taylor theorem: the velocity field $\mathbf{u}$ should not have velocity gradients in the z direction. Examination of the s and θ components of equation (5) also shows that a stream function description is available for the equatorial velocity $\mathbf{u}_e(s, \theta) = u_s \mathbf{e}_s + u_\theta \mathbf{e}_\theta$, namely

$$\mathbf{u}_e = \nabla \times (\Psi(s, \theta)\mathbf{e}_z) + u_0(s)\mathbf{e}_\theta, \tag{6}$$

where Ψ is the stream function of nonaxisymmetric equatorial motion, while u_0 is the axisymmetric

zonal flow. All variables are time-dependent, and the time variable is omitted for clarity.

[8] Within a spherical shell, $\mathbf{u}_e$ cannot satisfy the boundary condition of nonpenetration, since any $\mathbf{e}_s$-directed flow will convert into a z-dependent, $\mathbf{e}_z$-directed flow at the boundaries. An ageostrophic term has to be included, and we look for solutions of the form:

$$\mathbf{u} = u_s(s,\theta)\mathbf{e}_s + u_\theta(s,\theta)\mathbf{e}_\theta + \frac{dL}{ds} f(s,\theta,z)\mathbf{e}_z. \tag{7}$$

where f is a function of all three space variables and L is half the height of a fluid column

$$L = \sqrt{r_e^2 - s^2} \tag{8}$$

The derivative of L is therefore the local outer boundary slope. The quasigeostrophic model as a perturbation expansion of a geostrophic basic state would require $dL/ds \ll 1$. However, this model has been widely used (see for instance [*Busse*, 1970; *Cardin and Olson*, 1994]) without restriction on the magnitude of the boundary slope, often with strikingly good agreement with existing theories and experiments.

2.1. Nonaxisymmetric Motion

[9] We now examine nonaxisymmetric (or convective) motion, for which radial flow is nonzero, and zonal-averaged flow is zero. Taking the curl of equation (1) yields

$$\frac{\partial \boldsymbol{\omega}}{\partial t} + (\mathbf{u}\cdot\nabla)\boldsymbol{\omega} - (\boldsymbol{\omega}\cdot\nabla)\mathbf{u} - 2E^{-1}\frac{\partial \mathbf{u}}{\partial z} = \nabla^2\boldsymbol{\omega} + Ra\, s\, \nabla\times(T\mathbf{e}_{zs}), \tag{9}$$

$\boldsymbol{\omega} = \nabla \times \mathbf{u}$ being the flow vorticity. Taking the z component of (9) yields

$$\frac{\partial \omega}{\partial t} + (\mathbf{u}_\mathbf{e}\cdot\nabla_e)\omega - \left(2E^{-1} + \omega\right)\frac{\partial u_z}{\partial z} = \nabla_e^2\omega + Ra\frac{\partial T}{\partial \theta}, \tag{10}$$

where $\omega(s, \theta) = \boldsymbol{\omega}\cdot\mathbf{e}_z$ is the axial vorticity, u_z is the $\mathbf{e}_z$-directed velocity and

$$\nabla = \nabla_e + \frac{\partial}{\partial z}. \tag{11}$$

The Rossby number is assumed to be small and therefore $\omega \ll 2E^{-1}$. We average equation (10) in the z direction using operator

$$[\,]_z = \frac{1}{2L}\int_{-L}^{L} dz, \tag{12}$$

We define

$$T_0 = [T]_z. \tag{13}$$

The z-averaging does not affect the z independant variables, and the resulting equation is

$$\frac{\partial \omega}{\partial t} + (\mathbf{u}_\mathbf{e}\cdot\nabla_e)\omega - \frac{2E^{-1}}{2L}(u_z(L) - u_z(-L)) = \nabla_e^2\omega + Ra\frac{\partial T_0}{\partial \theta}. \tag{14}$$

To express the vertical velocity $u_z(L)$ we write the nonpenetration condition at the outer boundary, modified to take into account the Ekman pumping through the boundary layer [*Gubbins and Roberts*, 1987, p. 95]:

$$\mathbf{u}\cdot\mathbf{n} = \frac{1}{2}E^{1/2}\mathbf{n}\cdot\nabla\times\left[\frac{1}{\sqrt{|\mathbf{n}\cdot\mathbf{e}_z|}}\left(\mathbf{n}\times\mathbf{u} - \frac{\mathbf{n}\cdot\mathbf{e}_z}{|\mathbf{n}\cdot\mathbf{e}_z|}\mathbf{u}\right)\right] \tag{15}$$

where $\mathbf{n}$ is the normal to the outer boundary pointing outward (see Figure 1). $\mathbf{u}\cdot\mathbf{n}$ can also be written

$$\mathbf{u}\cdot\mathbf{n} = u_s\mathbf{n}\cdot\mathbf{e}_s + u_z(L)\mathbf{n}\cdot\mathbf{e}_z \tag{16}$$

Solving for $u_z(L)$ in (15) and (16) gives

$$u_z(L) = \frac{dL}{ds}u_s + \frac{E^{1/2}}{2\mathbf{n}\cdot\mathbf{e}_z}\mathbf{n}\cdot\nabla\times\left[\frac{1}{\sqrt{|\mathbf{n}\cdot\mathbf{e}_z|}}\left(\mathbf{n}\times\mathbf{u} - \frac{\mathbf{n}\cdot\mathbf{e}_z}{|\mathbf{n}\cdot\mathbf{e}_z|}\mathbf{u}\right)\right] \tag{17}$$

The Ekman pumping contribution in (17) is typically $E^{1/2}$ times weaker than the slope-induced circulation, and is therefore neglected. Moreover, we have $u_z(-L) = -u_z(L)$. Equation (14) then becomes

$$\frac{\partial \omega}{\partial t} + (\mathbf{u}_\mathbf{e}\cdot\nabla_e)\omega - E^{-1}\frac{2}{L}\frac{dL}{ds}u_s = \nabla_e^2\omega + Ra\frac{\partial T_0}{\partial \theta}, \tag{18}$$

which is rewritten using the total equatorial time derivative $d/dt = \partial/\partial t + (\mathbf{u}_e\cdot\nabla_e)$:

$$\frac{d}{dt}\left(\omega - 2E^{-1}\ln L\right) = \nabla_e^2\omega + Ra\frac{\partial T_0}{\partial \theta}. \tag{19}$$

in order to highlight the role of the potential vorticity $q = \omega - 2E^{-1}\ln L$. Equation (19) is

analogous to the beta-plane equation used in ocean and atmosphere dynamics (see for instance [*Pedlosky*, 1987]).

2.2. Axisymmetric Motion

[10] We now examine the axisymmetric, or zonal component of motion $u_0(r) = \mathbf{e}_\theta \cdot [\mathbf{u}]_{z,\theta}$. For this we project (1) in the θ direction and apply the zonal averaging operator, which makes the pressure gradient identically disappear:

$$\frac{\partial u_0}{\partial t} + \left[(\mathbf{u}\cdot\nabla)u_\theta + \frac{u_s u_\theta}{s}\right]_{z,\theta} + 2E^{-1}\mathbf{e}_\theta \cdot [\mathbf{e}_z \times \mathbf{u}]_{z,\theta} = \nabla_e^2 u_0 - \frac{u_0}{s^2}. \tag{20}$$

The only forcing term for geostrophic zonal flow is the zonal component of Reynolds stresses, which is independent of z. The Coriolis term is the flux of u_s through a cylinder coaxial with $\mathbf{e}_z$, of radius s, contained within the spherical outer boundary. The fluid is incompressible, and therefore this flux is the opposite of the flux through the spherical caps above and below this cylinder, which can readily be expressed using the Ekman pumping formula (15). Simple vector algebra yields:

$$2E^{-1}\mathbf{e}_\theta \cdot [\mathbf{e}_z \times \mathbf{u}]_{z,\theta} = \frac{E^{-1/2}}{L\sqrt{|\mathbf{n}\cdot\mathbf{e}_z|}} u_0, \tag{21}$$

Equation (20) finally becomes:

$$\frac{\partial u_0}{\partial t} + \left[(\mathbf{u}_e\cdot\nabla_e)u_\theta + \frac{u_s u_\theta}{s}\right]_\theta + \frac{E^{-1/2}}{L\sqrt{|\mathbf{n}\cdot\mathbf{e}_z|}} u_0 = \nabla_e^2 u_0 - \frac{u_0}{s^2}. \tag{22}$$

For typical $O(1)$ radial scales of the zonal flow variation, the Ekman friction term in equation (22) is presumably much larger than the viscous diffusion term. The Ekman friction term was omitted by [*Cardin and Olson*, 1994], resulting in a very large zonal flow that was not present in the experiments.

[11] In the present analysis, a distinction is made between the $m = 0$ mode, for which boundary layer friction dominates, and all other modes, for which volume friction dominates. As the system goes into a nonlinear regime, low m nonaxisymmetric modes could also be influenced by boundary layer friction, and a physically more relevant analysis would need to include its contribution. However, Ekman friction is mathematically less tractable for nonaxisymmetric modes than for the axisymmetric mode, and the distinction we have made is a choice of simplicity which, as we will see later, captures the essential features of nonlinear convection.

2.3. Thermal Equation

[12] To obtain the equation for T_0 we apply the $[\ ]_z$ averaging operator on (2):

$$\frac{\partial T_0}{\partial t} + [(\mathbf{u}\cdot\nabla)T]_z = P^{-1}\left(\nabla_e^2 T_0 + \frac{\partial T}{\partial z}(L) - \frac{\partial T}{\partial z}(-L)\right), \tag{23}$$

and we have

$$[(\mathbf{u}\cdot\nabla)T]_z = (\mathbf{u}_\mathbf{e}\cdot\nabla_e)T_0 + [u_z\frac{\partial T}{\partial z}]_z. \tag{24}$$

Temperature gradients parallel to the rotation axis result into thermal winds in the zonal direction. These winds cannot be described within the quasigeostrophic framework, since the z structure of the temperature field is not solved. This is however not crucial, since in large forcing situations, the zonal part of motion that arises from Reynolds stresses dominates over thermal winds [*Aubert et al.*, 2001; *Christensen*, 2002]. We choose not to describe these effects and therefore neglect z-gradients of temperature in (23) and (24) to obtain

$$\frac{\partial T_0}{\partial t} + (\mathbf{u}_e\cdot\nabla_e)T_0 = P^{-1}\nabla_e^2 T_0. \tag{25}$$

2.4. Numerical Method

[13] The system (19, 22, 25), altogether with the stream function definition (6) is closed for the unknown fields Ψ, T_0 and u_0. These are expanded into Fourier components in the azimuthal direction, up to degree $m = 2048$ ($m = 0$ being the zonal flow) for the most demanding calculations. As stated earlier, the no-slip boundary conditions are employed at boundaries. The explicit condition for the stream function Ψ of nonzonal modes is therefore

$$\Psi(r_i) = \Psi(r_e) = \frac{\partial\Psi}{\partial s}(r_i) = \frac{\partial\Psi}{\partial s}(r_e) = 0, \tag{26}$$

and the zonal velocity obeys the boundary conditions

$$u_0(r_i) = u_0(r_e) = 0. \tag{27}$$

A second-order finite-difference scheme is chosen with up to 400 grid points to solve the equations in the radial direction. The linear part of the equations is solved directly in the Fourier space using a Crank-Nicolson implicit integration scheme for the Coriolis force and the viscous diffusion terms, and an Adams-Bashforth explicit scheme for the buoyancy term. Nonlinear terms are computed in real space, and then transferred back in Fourier space, where they are integrated in an Adams-Bashforth scheme. The time step is fixed and has typical values of one hundred container revolutions. Nonlinear calculations are done with no assumption on the azimuthal symmetry of the solution. The two-dimensional code we are using is largely derived from the three-dimensional code validated in the benchmark test for spherical shell numerical dynamos by [*Christensen et al.*, 2001] under reference ACD.

3. Onset of Convection, Differential Heating

[14] In order to get some points of comparison with the existing numerical and theoretical studies, we look at the onset of the convective instability in the case $P = 1$ and $r_i/r_e = 0.35$. T_0 is decomposed into

$$T_0 = \Theta + T_{s2D} \tag{28}$$

where Θ is the temperature perturbation and T_{s2D} the static profile obeying

$$\nabla_e^2 T_{s2D} = 0. \tag{29}$$

The two-dimensional geometry would require to adopt the profile

$$T_{s2D} = \frac{\ln(s/r_i)}{P\ln(r_e/r_i)} \tag{30}$$

Since we are interested in comparing two- and three-dimensional situations, we adopt instead the z-averaged profile from the 3D static profile:

$$T_{s3D} = \left[\frac{r_e}{P(r_e - r_i)}\left(-\frac{r_i}{r} + 1\right)\right]_z \tag{31}$$

Table 1. Critical Parameters for $P = 1$, Differential Heating[a]

Dimension	E	Ra_c	m_c	w_c
3D	$4.73\ 10^{-3}$	$8.9\ 10^{3}$	3	2.99
3D	$4.73\ 10^{-4}$	$7.93\ 10^{4}$	5	16.43
3D	$4.73\ 10^{-5}$	$1.08\ 10^{6}$	9	232.4
3D	$4.73\ 10^{-6}$	$1.71\ 10^{7}$	19	1202
3D	$4.73\ 10^{-7}$	$3.01\ 10^{8}$	40	5914
2D	$4.73\ 10^{-3}$	$7.6\ 10^{3}$	3	16.54
2D	$4.73\ 10^{-4}$	$7.56\ 10^{4}$	6	88.1
2D	$4.73\ 10^{-5}$	$9.55\ 10^{5}$	11	385.1
2D	$4.73\ 10^{-6}$	$1.47\ 10^{7}$	21	1717
2D	$4.73\ 10^{-7}$	$2.56\ 10^{8}$	43	7766
2D	10^{-7}	$1.75\ 10^{9}$	70	21297
2D	10^{-8}	$3.55\ 10^{10}$	147	99137
2D/3D	$4.73\ 10^{-3}$	0.85	1	5.5
2D/3D	$4.73\ 10^{-4}$	0.95	1.2	5.36
2D/3D	$4.73\ 10^{-5}$	0.88	1.2	1.65
2D/3D	$4.73\ 10^{-6}$	0.86	1.11	1.42
2D/3D	$4.73\ 10^{-7}$	0.85	1.075	1.31

[a] For each Ekman number, the 2D/3D lines are computations of the ratio between 2D and 3D critical parameters.

with $r^2 = s^2 + z^2$. The result is

$$T_{s3D} = \frac{r_e}{P(r_e - r_i)}\left(-\frac{r_i}{L(s)}\operatorname{asinh}\left(\frac{L}{s}\right) + 1\right). \tag{32}$$

[15] Surprisingly enough, plotting profiles T_{s3D} and T_{s2D} versus cylindrical radius reveals that they superimpose quite remarkably by simple shifting and scaling operations, both of which have no consequence on the dynamics. This means that the consistency of the model is not affected if we adopt T_{s3D} as static temperature profile.

[16] For each Ekman number, the linear part of the simulation is then iterated to obtain the minimal value Ra_c (critical Rayleigh number) when one single mode m_c has zero growing rate, the other modes having negative growing rates. The pulsation w_c of this mode is also retrieved. Results for $P = 1$ are given in Table 1, and plotted on Figure 2. These two-dimensional results are compared with results obtained by (E. Dormy et al., The onset of thermal convection in rotating spherical shells, manuscript submitted to *Journal of Fluid Mechanics*, 2003, hereinafter referred to as Dormy et al., submitted manuscript, 2003) with a fully three-dimensional code, as well as theoretical calculations in the limit of vanishing E. The usual asymptotic laws for critical parameters [*Busse*, 1970; *Jones et al.*, 2000] are satisfied. The most striking result is

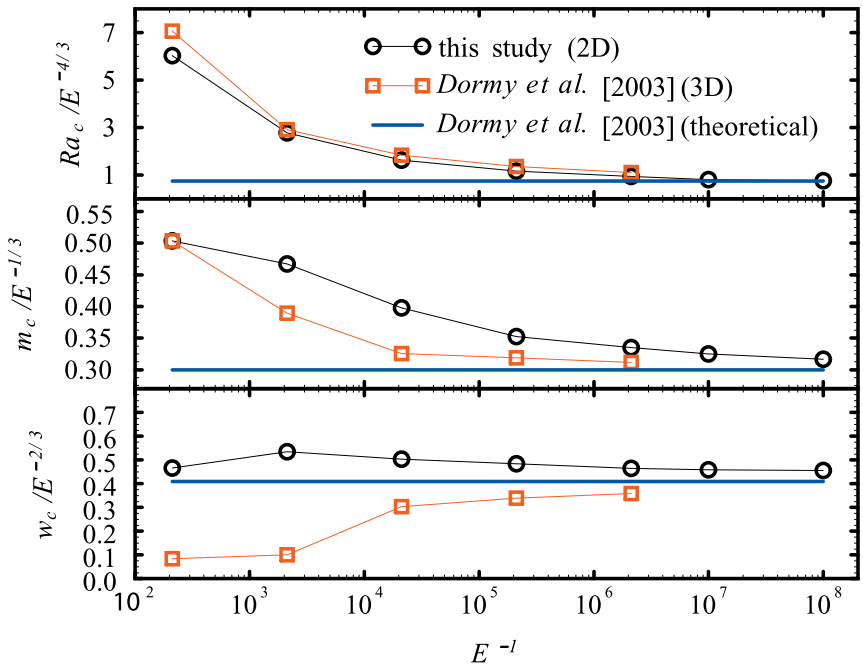

Figure 2. Behavior of critical Rayleigh number Ra_c, critical pulsation w_c, and critical mode number m_c as function of the inverse Ekman number, in the case of differential heating. Two-dimensional numerical solutions are compared with three-dimensional numerical solutions and an analytical solution for the $E \rightarrow 0$ limit (Dormy et al., submitted manuscript, 2003).

that the limit reached by 2D results is in excellent agreement with the limit reached by 3D results, and the theoretical prediction of (Dormy et al., submitted manuscript, 2003), which is an extension of the local theory of [*Roberts*, 1968; *Busse*, 1970] into the case of differential heating and no-slip boundary conditions.

[17] A structural comparison of two- and three-dimensional solutions is performed in the equatorial plane (Figures 3a and 3b). Apart from a difference of two units in the mode number, the solutions are remarkably similar. The radial structure of both solutions (zonal average of squared radial velocity and temperature perturbation) is

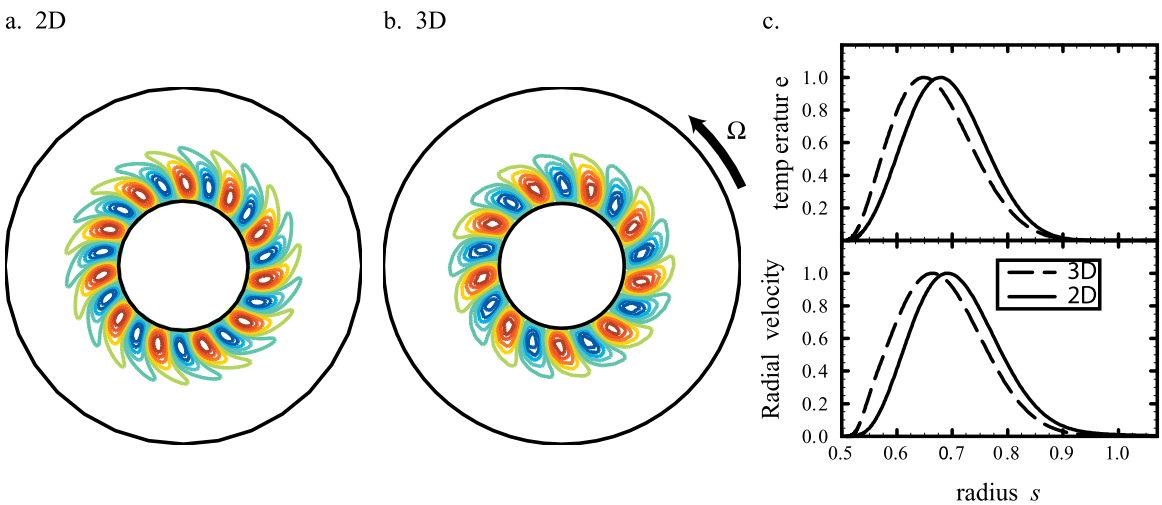

Figure 3. (a) Radial velocity plot of the linear solution in equatorial plane, obtained with the quasigeostrophic approximation. (b) Same plot for a full three-dimensional solution. (c) Comparison of the structure of azimuthal average for the squared radial velocity and the temperature perturbation. $E = 4.73\ 10^{-5}$, $P = 1$.

shown more precisely in Figure 3c. Solutions mainly differ in their behavior near the inner boundary.

[18] While this boundary is modeled as a cylinder in the 2D case, it is a sphere in the 3D model. The boundary layer structure of the two cases are therefore different. Solutions also differ in the s-location of their maximum. [*Zhang and Jones*, 1993] have shown that when the Ekman friction of convective cells is neglected, the pulsation and critical latitude of the solution are modified. In our model this Ekman friction is precisely neglected for nonzonal modes, while it is kept for the zonal mode. This can explain the discrepancy for the radial location of the solution maximum and for the critical pulsation. For the latter variable the effect disappears, as expected, at low Ekman numbers. The radial extent of the solution scales with $E^{0.2}$, in agreement with what was found by [*Cardin and Olson*, 1994]. This is compatible with the 2/9 exponent of the local theory of [*Roberts*, 1968].

4. Finite Amplitude Convection

4.1. Introduction and Notations

[19] The convection of finite amplitude is now examined, in the case of differential heating, which has proven to provide a satisfactory quantitative agreement at the onset. This study is closely related to the experimental work of [*Aubert et al.*, 2001]. Calculations have been carried out for Prandtl numbers $P = 7$ and $P = 0.025$, describing respectively experiments done in water and liquid gallium, and for the aspect ratio $r_i/r_e = 4/11$ of the experimental set-up.

[20] We first define some useful scalar properties of the flow: the energy of nonaxisymmetric modes of convection E_{conv} is

$$E_{conv} = \frac{1}{\pi(r_e^2 - r_i^2)} \int\int \left(u_s^2 + u_\theta^2\right)_{m\neq 0} s ds d\theta \qquad (33)$$

The mean, time averaged radial velocity U_s of the fluid, which is also the Reynolds number of the flow, is then given by

$$U_s = \sqrt{[E_{conv}]_t}, \qquad (34)$$

The zonal energy, or energy present in the axisymmetric mode of convection, is defined as

$$E_{zon} = \frac{1}{\pi(r_e^2 - r_i^2)} \int\int u_0^2 s ds d\theta, \qquad (35)$$

And the mean zonal velocity in the shell is

$$U_\theta = \sqrt{[E_{zon}]_t}. \qquad (36)$$

The Nusselt number of the flow is defined as

$$Nu = \frac{[\partial T/\partial r]_{\theta,t}(r_i)}{\partial T_{s3D}/\partial r(r_i)}. \qquad (37)$$

[21] The Rossby number can be written $Ro = U_s E$, and it never exceeds 10^{-2} in our numerical simulations.

4.2. Dynamics of Potential Vorticity

[22] Equation (19) shows that the potential vorticity (hereafter noted as PV) $q = \omega - 2E^{-1} \ln L$ is an advected quantity whose conservation is only affected by buoyancy and viscosity. Figure 4a shows a color-coded image of q in a highly forced situation for which the Reynolds number is 3700. For better understanding of the dynamics a movie file corresponding to this plot is proposed the first animation (see dynamic content in the HTML version of the article). In Figure 4d the azimuthal average of some properties is also presented. The thermal instability is mostly active near the inner boundary of the model, where strong radial currents exist (see lower plot of Figure 4d).

[23] A ring of anticyclones ($\omega < 0$) is clearly visible on Figure 4a, near the inner boundary. Further away toward the outer boundary, structures are of cyclonic type, and weaker. Figure 4c explains the origin of this spatial separation of vorticity structures, which has previously been observed by [*Aubert et al.*, 2002] in similar rotating fluid experiments, and is a general property of fluid motion over a beta-plane. In this plot a vortex (in black) induces a displacement (in red) in the surrounding fluid. By evolving at constant PV, the surrounding fluid acquires excess vorticity (small blue vortices) of one sign on the prograde side of the vortex, and of the opposite sign on the retrograde side of the vortex. The net back-reaction

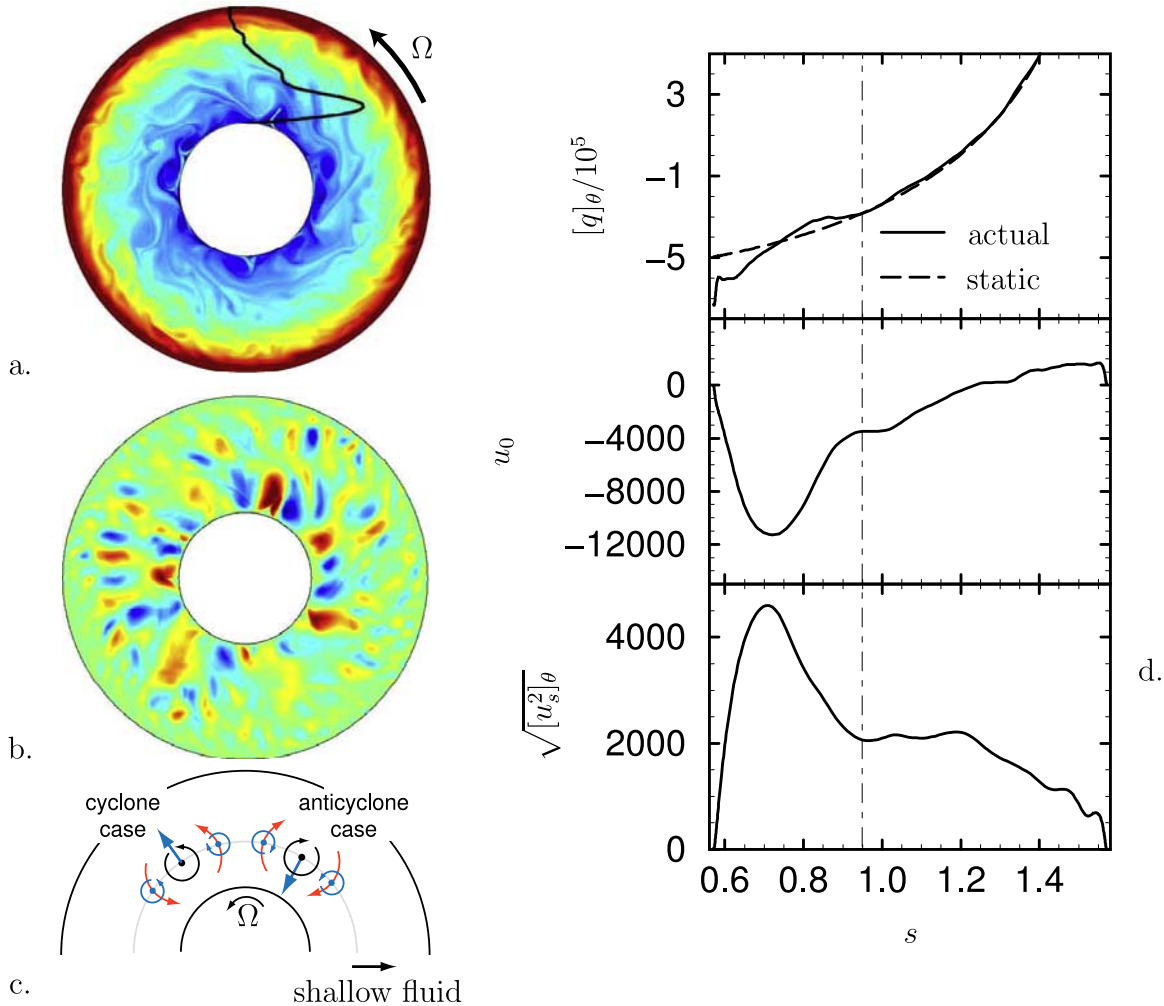

Figure 4. (a) Potential vorticity map (rainbow colormap from $-8\ 10^5$, blue to $1.3\ 10^6$, red) for a calculation at $P = 0.025$, $E = 1.46\ 10^{-6}$, $Ra = 5\ Ra_c$. Reynolds number is 3700. Black line is the zonal flow, mostly retrograde, with maximal negative amplitude of −11250. (b) Radial velocity map (rainbow from -10^4 to 10^4) for the same situation. (c) Sketch explaining the separation of cyclones and anticyclones. (d) Mean static and actual potential vorticity profiles (upper plot), zonal flow (middle plot), and root-mean square zonal average of radial velocity (also Reynolds number based on the local velocity), as function of radius. The dot-dashed line marks the limit of the region where the actual potential vorticity profile departs significantly from its value when the fluid is at rest.

of the induced vorticity on the original vortex (in blue) is a radial current which displaces anticyclones toward deep fluid and cyclones toward shallow fluid.

[24] The rms radial velocity in lower plot of Figure 4d can be seen as a local Reynolds number. This number is large in the region where anticyclones and cyclones have been separated, and inertia has full influence here. In particular, a strong zonal flow (black line on Figure 4a and also drawn on middle plot of Figure 4d) advects this inertial ring in the retrograde direction. Vortex dynamics in this zone is very reminiscent of 2D turbulence, with very frequent vortex mergers between like-signed structures. Evidence of vortex filament stretching can also be seen on Figure 4a. Those two observations support the usual phenomenology [*Rhines*, 1975] in terms of energy flux toward large scales and enstrophy flux toward small scales.

[25] In contrast, at larger radii, and near the outer boundary, the large spherical boundary slope dL/ds constrains the flow to be much weaker, a conse-

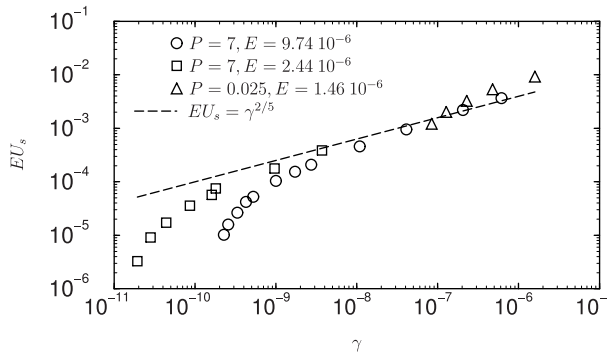

Figure 5. Numerical test of the scaling relation of [*Aubert et al.*, 2001] for fully developed convective motions.

quence of the Proudman-Taylor constraint (see again lower plot of Figure 4d). At these radii, rather regular structures drift in the prograde direction (see the alternating blue and yellow patches near the outer boundary on Figure 4b, and movie 1). A careful examination of zonal flow at the same location shows that the drift is 80% propagative, the structures are therefore Rossby waves excited by the inertial ring. The local dynamics therefore depend on the geographical position in the shell. More detail on the transition between inertial structures and Rossby waves will be given in the next section.

[26] From the PV conservation mechanism which gives birth to the anticyclonic ring, [*Aubert et al.*, 2001] have derived a scaling relation for highly forced rotating thermal convection, which was successfully tested versus their experimental data, and later also agreed with three-dimensional numerical simulations [*Christensen*, 2002]:

$$EU_s \propto \gamma^{2/5} \tag{38}$$

where $\gamma = Ra_Q E^3 P^{-2}$ and $Ra_Q = RaNu$ is the heat-flux based Rayleigh number. This scaling relation applies to large forcing, and indeed the γ parameter does not depend on the various diffusivities of the system. Figure 5 presents a test of (38) versus our numerical data set. When the flow forcing is large enough the numerical data approach an asymptote correctly described by $\gamma^{2/5}$, with a prefactor close to 1 in all cases. The law is therefore valid for the quasigeostrophic model, and suggests that a point-to-point comparison with experiments, as well as with three-dimensional numerical simulations, is possible.

[27] A strong retrograde zonal flow exists in the numerical simulation of Figure 4a. This has already been observed experimentally [*Sumita and Olson*, 2000; *Aubert et al.*, 2001]. [*Aubert et al.*, 2002] explained the origin of this zonal flow in terms of potential vorticity mixing. We give here a brief account of their demonstration, adapted to the case of rotating convection.

[28] When there is no motion in the shell a static PV profile $q_s(s)$ exists (dashed line in upper plot of Figure 4d):

$$q_s(s) = -2E^{-1} \ln L(s) \tag{39}$$

In a context of material PV conservation and strong radial motions, this profile gets mixed into a new profile $[q]_\theta(r)$. The solid line in the upper plot of Figure 4d presents this profile for the numerical simulation of Figure 4a. As expected, profiles $q_s(s)$ and $[q]_\theta(r)$ differ significantly only in the region with strong radial motions and therefore strong mixing (left of the dot-dashed vertical line in Figure 4d). In this region the mixed profile has developed two flattened regions, corresponding to the mixing effect of anticyclones (near $s = 0.6$) and cyclones (near $s = 0.9$). The PV gradient setting up around $s = 0.7$ is therefore a consequence of the separation of vorticity structures induced by the beta-plane.

[29] The Stokes theorem allows to mathematically relate the mean zonal circulation shown in Figure 4a and the zonal average of vorticity, which is also the difference between static and mixed profile observed in Figure 4d:

$$u_0 = \frac{1}{s}\int_{s_i}^{s} s[\omega]_\theta ds = \frac{1}{s}\int_{s_i}^{s} s([q]_\theta - q_s) ds \tag{40}$$

Vortex separation and PV mixing therefore automatically produce a mean zonal flow.

[30] The direction of zonal flow is retrograde because the mixed PV level closest to the inner boundary is lower than the static profile; this feature is completely determined by the geometry.

[*Aubert et al.*, 2002] made another important prediction: if potential vorticity is conserved on average, then in the limit of infinite mixing, profile $[q]_\theta$ will reach a definitive shape which will be constrained by the geometry. In other words, the mixing extracts PV from the planetary reservoir, and this reservoir has a limited capacity. Consequently, there exists a saturation value U_∞ for U_θ. Even though it is complicated to have a precise expression for U_∞, [*Aubert et al.*, 2002] have proposed a simplified expression $U_\infty \approx E^{-1}\delta^2$, where δ is the (geometrically constrained) length of the mixing region. The potential vorticity reservoir indeed has more capacity when the system rotates faster.

[31] The theory of [*Aubert et al.*, 2002] has been developed to apply to situations where the PV is rigorously conserved. This is not exactly true in the present case, and it is somewhat complicated to estimate how much PV is injected by buoyancy, and how much is withdrawn due to molecular viscosity. However, the conservative theory is a useful guideline to understand the features of the nonconservative case. Moreover, some evidence of zonal flow saturation in the case of rotating convection can be found on Figure 6, which reproduces the last figure of [*Aubert et al.*, 2002]. U_θ/U_∞ (here we have taken a constant length $\delta = 1/7$ for the mixing region) is plotted against the ratio between the Ekman spin-up time $\tau_E = E^{1/2}$ and the turnover time $\tau_\omega = d/U_s$, where d is the typical vortex size. This ratio quantifies the relative importance of Ekman friction, which prevents mixing, and convective motion, which favours mixing. At low forcing ($\tau_E \ll \tau_\omega$) the generation of a zonal flow is usually connected to the action of the zonal component of Reynolds stresses [*Cardin and Olson*, 1994; *Sumita and Olson*, 2000; *Christensen*, 2002]. From this a rough scaling can be derived [*Aubert et al.*, 2001], which assumes a perfect correlation between the radial and zonal component of equatorial velocity:

$$U_\theta \propto U_s^2 \tag{41}$$

The data set shows significant departure from (41) when the mixing becomes strong ($\tau_E \gg \tau_\omega$), and an inflexion such that U_θ never exceeds its perfect mixing value. Owing to numerical computing limitations it was not possible to compute beyond the value $\tau_E/\tau_\omega = 100$, where Reynolds numbers were already of order 5000.

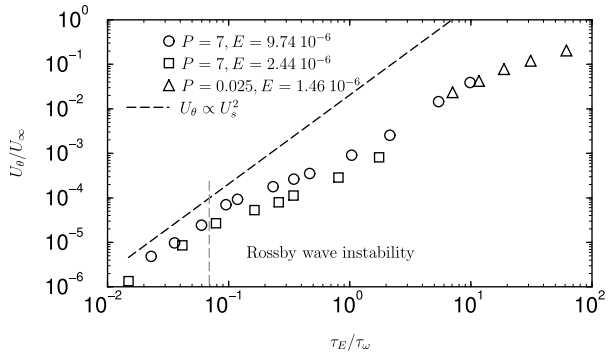

Figure 6. Evolution of zonal motion versus the mixing parameter τ_E/τ_ω. The system departs from the dependency $U_\theta \propto U_s^2$. The vertical dashed line marks the approximate threshold for the instability of the Rossby wave state.

4.3. Evolution of the System With the Reynolds Number

[32] Having described the onset of convection, and an highly forced state, we now turn to the description of what lies in-between. From the previous discussion the Reynolds number appears as an obvious parameter to describe the dynamical evolution, without considering the thermal source, which will be studied later in more detail. Figure 7 displays four stream function plots at various values of the Reynolds number U_s. Figure 7a is a situation close to the onset, with little radial advection, and the flow is mainly a Rossby wave, whose amplitude is saturated by nonlinear effects. The regular pattern of the wave is stable. Zonal motion, which is also reported in Figure 7a, is a consequence of the action of Reynolds stresses on this well-organized flow pattern, and, as can be seen on Figure 6, law (41) holds. Figure 7b has a stronger value of U_s and therefore stronger radial advection; as a consequence, spatial separations occurs between cyclones and anticyclones due to the beta-plane effect, and the Rossby wave is made unstable. Good correlation in the Reynolds stresses is lost and the system has reached the point where it departs from law (41). On Figure 6 a vertical line marks this transition. It

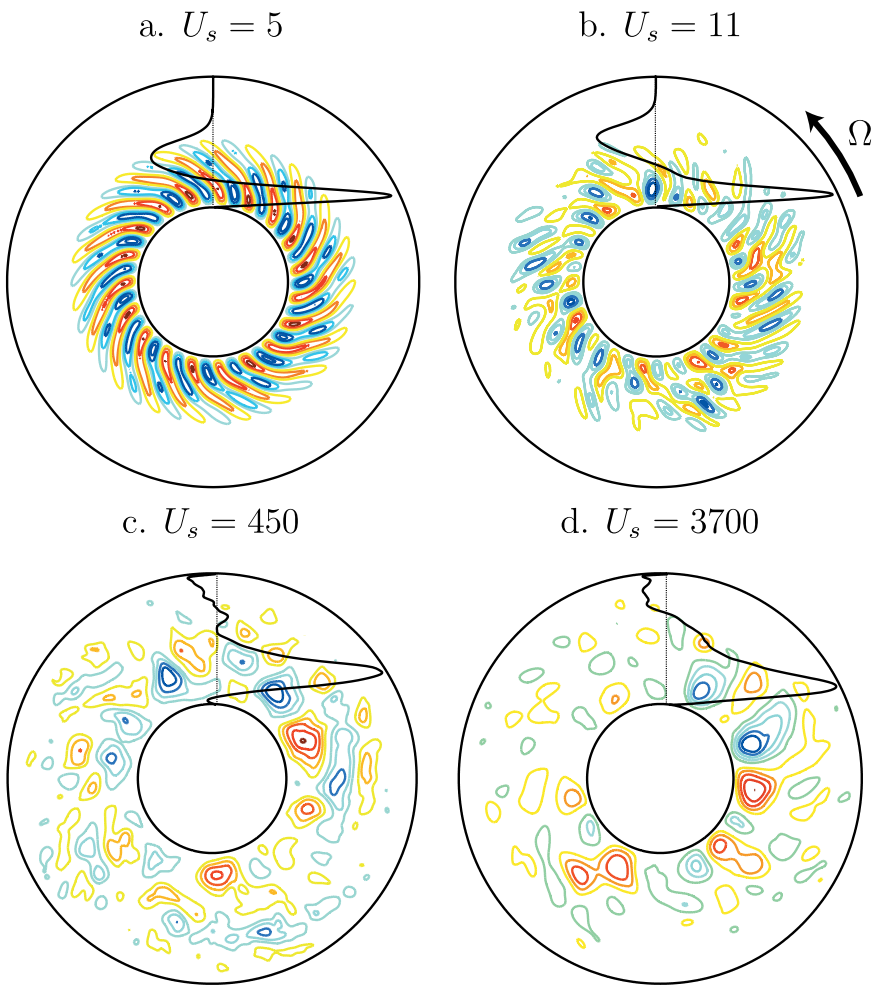

Figure 7. Stream function plots, all obtained for $P = 7$, $E = 9.7\ 10^{-6}$ except d., obtained for $P = 0.025$, $E = 1.46\ 10^{-6}$, showing the evolution of the system as the Reynolds number increases. Black lines are zonal flows, mostly retrograde with minima values of (a) −1.3, (b) −3, (c) −500, and (d) −11000.

may be quantified by the following criterion: the Rossby wave becomes unstable when the vortex turnover time τ_ω equals the wave period m_c/w_c. Using the asymptotic laws for m_c and w_c, this leaves a weak dependance in the parameter τ_E/τ_ω of Figure 6 for the destabilization of the Rossby wave:

$$\tau_E/\tau_\omega \propto E^{1/6}. \tag{42}$$

The condition (42) shows that the Rossby wave is more easily destabilized at low Ekman numbers. This is in agreement with Figure 6: at $P = 7$ the squares (low E) depart from law (41) before the circles (higher E). The destabilization condition can also be used to clarify an issue of the previous section: it gives the local Reynolds number at which Rossby waves cease to exist and inertial structures rise. It therefore describes the radius in the shell at which a transition occurs between inertial structures and Rossby waves.

[33] All four plots in Figure 7 show a general growth in convection cell size with the Reynolds number. This phenomenon has been previously observed in the experiments of [*Aubert et al.*, 2001]. It is a classical phenomenon: the conservation of potential vorticity in a beta-plane environment is a balance between inertia and Coriolis force, and this selects a length scale in the system known as the Rhines length scale [*Rhines*, 1975]:

$$d \propto \sqrt{U_s E \left(\frac{dL}{ds}\right)^{-1}} \tag{43}$$

This law is in qualitative agreement with the plots shown on Figure 7. The increase in cell size is a nontrivial feature of the system, which highlights the role of inertia (potential vorticity advection). A system dominated by viscosity would indeed select smaller scales as forcing increases, in order to dissipate energy. Here, as [*Aubert et al.*, 2001] noted, most of the energetic dissipation occurs through Ekman friction of zonal flow, and the inertia dominates dissipation for the nonzonal modes.

4.4. Thermal Structures

[34] The thermal evolution of the flow can be represented by plotting the Nusselt number as a function of the Péclet number $Pe = PU_s$ (Figure 8a). Numerical experiments performed at very different Prandtl number collapse on the same curve. The Nusselt number has little growth on one decade of Péclet number, and then starts to grow much more significantly. Careful observation of the temperature field allows to draw a possible interpretation for this change of behavior: at low forcing (Figure 8b), the thermal instability develops first near the inner boundary of the shell, where the static temperature profile has the steepest slope. The vortices associated with the convective motion mix heat and this flattens the temperature profile as forcing grows. As a result, large temperature gradients start to develop in the thermal boundary layer which forms next to the outer boundary of the shell. This layer ultimately becomes unstable and this triggers an external thermal instability which is visible in Figure 8c. A dual convective system sets up with plumes originating from both boundaries, the sinking plumes being weaker than the rising plumes due to the spherical geometry and the combined effect of Proudman-Taylor constraint and large dL/ds at the outer boundary.

[35] The birth of a thermal instability near the outer boundary, and of the associated plumes presumably increases the efficiency of the convective engine, and this can explain the increased slope in the *Nu-Pe* graph. Dual convective instability has been first observed in experiments by [*Sumita and Olson*, 2000], and plot 8.c is strikingly similar to their dye photographs. The external thermal instability is

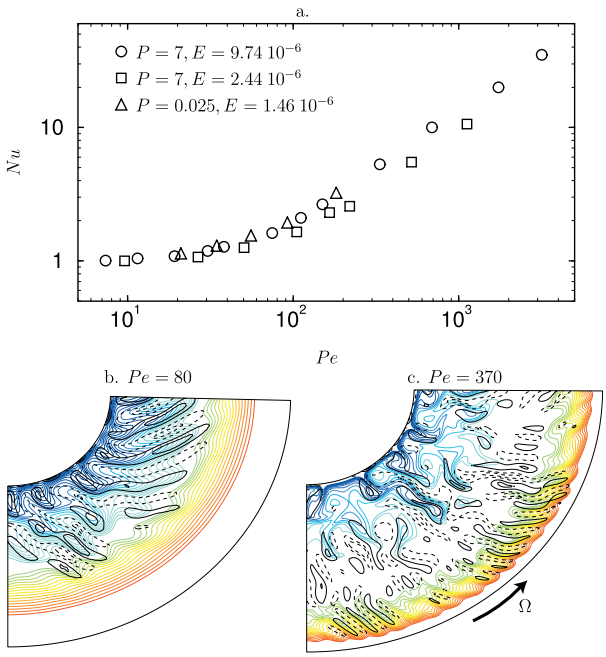

Figure 8. (a) Nusselt number as a function of the Peclet number. (b, c) Isothermal (colors) and vorticity (black, dotted lines are cyclones) lines below and above the external thermal instability onset. $E = 9.7\ 10^{-6}$, $P = 7$.

another source which, together with convective motion deeper in the shell, can excite the Rossby waves we have observed near the outer boundary.

5. Detailed Comparison With Doppler Measurements

[36] [*Aubert et al.*, 2001] performed the first systematic quantitative velocity measurements on rotating convection. The experimental set-up (Figure 9a) was a traditional centrifugal gravity experimental device, as pioneered by [*Busse and Carrigan*, 1976]. A sphere of radius 110 mm, filled with either water or liquid gallium, could be spun up to speeds of order 1000 rpm. The sphere was transversed by a cylinder of radius 40 mm, coaxial with the rotation axis. The inner cold temperature was fixed by circulating cold water through the inner cylinder, while the whole device was put in a hot thermostatic chamber to set the outer temperature. Both thermal gradient and gravity are the same as in the numerical simulation, and reversed when compared to the Earth's core situation, but

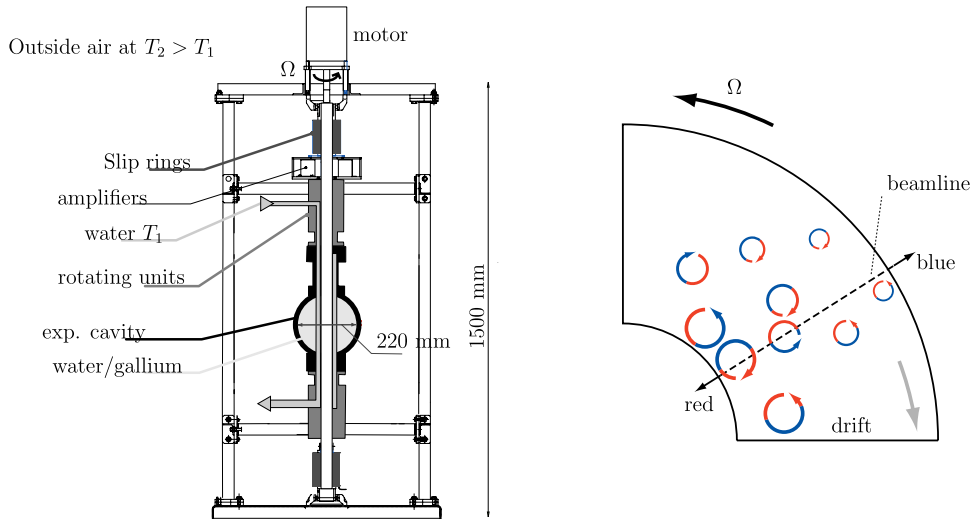

Figure 9. (a) Sketch of the experimental device. (b) Sketch explaining the ultrasonic Doppler velocimetry measurements in the equatorial plane. After [*Aubert et al.*, 2001].

buoyancy remains the same since it is the product of the two.

[37] Measurement technique was ultrasonic Doppler velocimetry [*Brito et al.*, 2001]. An ultrasonic transducer was embarked on the rotating sphere, attached in the equatorial plane, shooting toward the center of the device along a radial ray (see Figure 9b). The transducer fired ultrasonic bursts in the fluid, which was seeded with acoustically scattering particles. From the time delay of backscattered waves the position of the reflecting particle along the radial beam could be retrieved. From the Doppler shift the radial velocity component of the particle was also accessible. It was therefore possible to obtain radial velocity profiles at quite frequent time intervals (of order one tenth of a second). Imaging was performed as follows: each radial velocity profile was color-coded (red for a velocity flowing inward to the center of the device, blue for a velocity outward), and all profiles were stacked in a time-depth representation where the succession of colored spots shows the convection columns drifting across the beamline, under the combined influence of wave propagation and advection by zonal flow.

[38] Several key features of the Doppler maps obtained this way by [*Aubert et al.*, 2001] remained unexplained due to uncertainty on how and why structures passed along the ultrasonic transducer. These uncertainties can be cleared by point-to-point comparison with our numerical model, which can reach the parameters used in the experiment, and can output synthetic Doppler maps. Movie 2 in this paper explains the generation of such maps. An equatorial animation of radial velocity is shown on the right-hand side, with an horizontal white radial line marking the ultrasonic ray. On the left-hand side a Doppler map is produced as time goes by and as structures pass along the shooting line.

[39] However, a relevant control parameter has to be found first. The temperature difference- and heat flux- based Rayleigh numbers cannot do a good job because heat transport is three-dimensional in the experiments and two-dimensional in the numerics. Thus a given Rayleigh number will describe very different experimental and numerical configurations. In contrast, the discussion of the nonlinear study has highlighted the role of the Reynolds number, and, more precisely, of the root-mean square radial velocity profile, which can be seen as a local Reynolds number profile. In this section we choose to compare experiments and numerics with comparable rms velocity profiles, and then compare their other features such as the type of structures, time and length scales in Doppler maps, and the magnitude of zonal flow (when measurable).

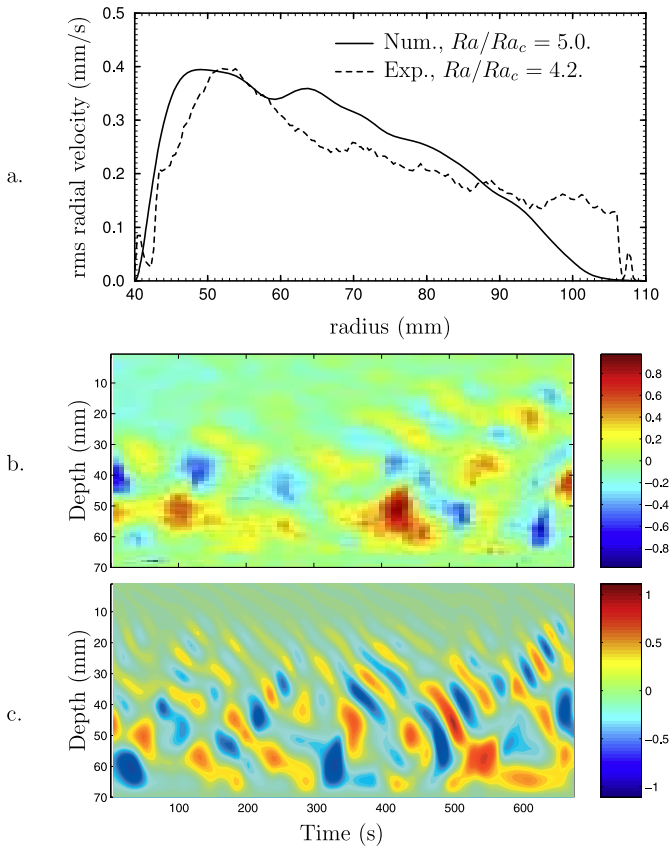

Figure 10. (a) The rms radial velocity profile (local Reynolds number profile) helps to choose a numerical simulation to compare to a given experience. (b) Experimental Doppler map, with velocities in mm/s. (c) Numerical synthetic Doppler map (velocities have been redimensioned in mm/s). $E = 9.74\ 10^{-6}$, $P = 7$.

[40] Figure 10 presents a situation based on an experiment performed in water at low thermal forcing, for which the Reynolds number is 20. The best corresponding rms radial velocity profile comes from a numerical experiment at a slightly higher forcing, very similar to the experiment shown in Figure 7b. The numerical situation lies beyond the Rossby wave destabilization limit, where a prograde-drifting Rossby wave has already been perturbed by inertia and a weak retrograde zonal flow. This comparison gives support to the existence of Rossby wave destabilization, and allows to explain the structure of the experimental profile. Shapes in Doppler profiles compare indeed quite interestingly: as seen on the Movie 2, the slanted bands near the outer boundary represent the Rossby wave, and larger patches near the inner boundary represent the inertial vortices that are starting to form here. The patches are larger because their prograde drift is slowed down by a retrograde zonal flow. The time scale for the Rossby wave drift is quite faster in numerics when compared to experiments. This is a consequence of neglecting Ekman friction for Rossby modes, as noted first by [*Zhang and Jones*, 1993]. As seen in our linear study, this discrepancy vanishes at vanishing E. Along a slanted band, the Rossby wave amplitude has modulations with one or two nodes, both in the experimental and synthetic Doppler maps. These are the consequence of Rossby wave destabilization, as seen in Figure 7b. In this situation, the zonal flow amplitude given by the numerics is very small, of the order of a tenth of millimeter per second. This lies below the Doppler system sensitivity threshold, and indeed [*Aubert et al.*, 2001] reported the zonal flow to be unmeasurable in this case.

[41] Figure 11 presents an experiment performed in water at the same rotation rate, but with higher thermal forcing, resulting in a Reynolds number of

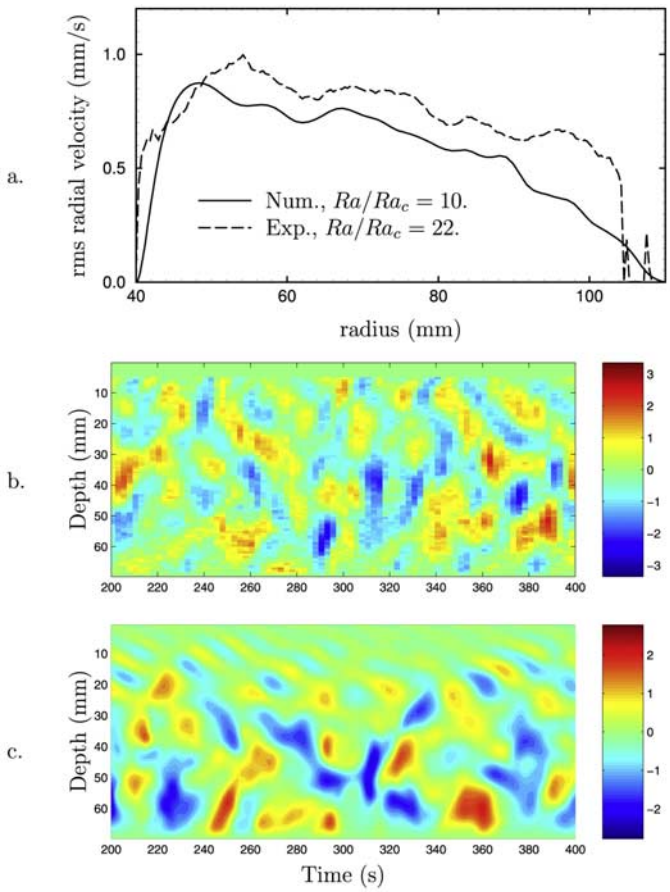

Figure 11. (a) The rms radial velocity profiles. (b) Experimental Doppler map. (c) Numerical synthetic Doppler map. $E = 9.74\ 10^{-6}$, $P = 7$.

approximately 50. The best corresponding numerical rms radial velocity profile was found at a very different Rayleigh number. The numerical and experimental Rayleigh number scales have therefore considerably diverged, suggesting that the heat flux is now completely different in the two- and three-dimensional situations. Although it has a lower Reynolds number, the numerical simulation is not very different from this depicted on Figure 7c. Here again the experiments and the numerics compare successfully. The present situation is more chaotic. The domain devoted to inertial structures has considerably grown in radial size, and Rossby waves can only be seen in the immediate vicinity of the outer boundary. Figures 10 and 11 therefore give strong support to the idea of coexistence of Rossby waves and inertial structures. The present comparison shows in addition that when the Reynolds number increases, the frontier between the two types of structures shifts toward the outer boundary. In contrast with the previous situation, the experimental and numerical time scales are in much better agreement. The dominant time scale in the system is now indeed the inertial time τ_ω, and not the time associated with Rossby wave drift.

[42] Figure 12 presents a situation based now on a liquid gallium experiment at high forcing. The Reynolds number is approximately 1000, and the matching numerical experiments is quite similar to this depicted in Figure 7d. Patches near the inner cylinder are now the most energetic part of the flow, they drift in the retrograde direction under the influence of a strong zonal flow, and a weak Rossby wave remains near the outer boundary. Comparison of Doppler profiles is satisfactory: time scales are compatible like in situation of Figure 11, patches size, distribution and shape

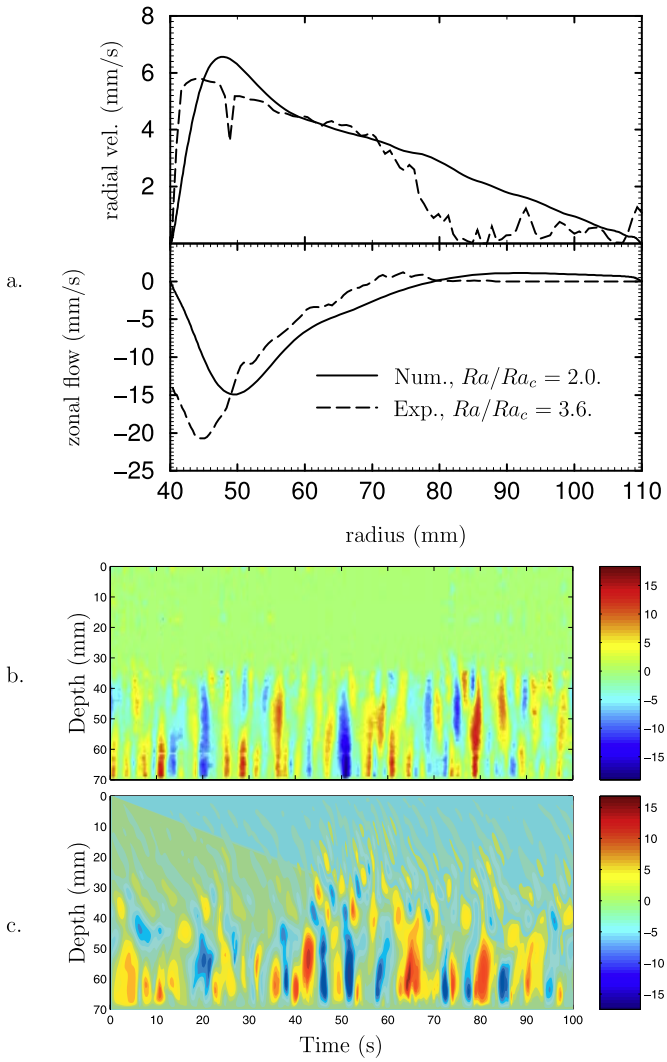

Figure 12. (a) The rms radial velocity and mean zonal flow plots. (b) Experimental Doppler map. (c) Numerical synthetic Doppler map. $E = 1.46\ 10^{-6}$, $P = 0.025$.

agree near the inner boundary. Unfortunately due to Doppler seeding problems one can not attest the presence of the weak Rossby wave in experiments.

[43] [*Aubert et al.*, 2001] reported a strong zonal flow in this case, although for technical reasons their experiments had underestimated the strength of the zonal flow, when compared to the more recent series of experiment from which Figure 12 was obtained. The numerical model is in very good agreement with the observations (Figure 12a). The strongly retrograde shape is similar in the experiment and in the simulation. The zonal wind measured in the experiment is however larger than the numerical prediction, and its maximum lies closer to the inner cylinder. Both differences can be attributed to the presence of a retrograde thermal wind in the experiment, which was evaluated by [*Aubert et al.*, 2001] to be approximately 5 mm/s. As previously discussed, thermal wind effects are likely to be present in thermally diffusive systems such as liquid metals, and are not described by the quasigeostrophic model. The largest part of zonal flow is nevertheless explained by potential vorticity mixing in the quasigeostrophic framework.

6. Discussion

[44] Many recurrent observations made in previous studies of rotating convection can be reproduced

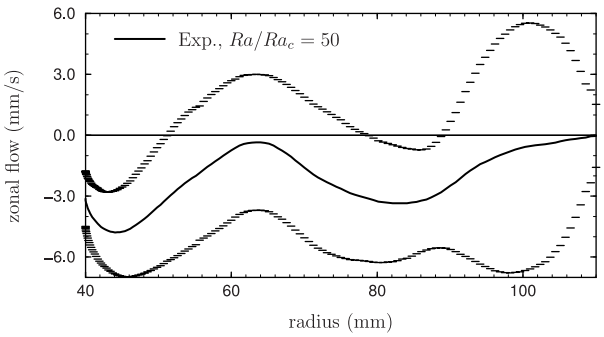

Figure 13. Experimental mean zonal flow for $P = 7$, $E = 6.5\ 10^{-6}$ and $Ra = 50\ Ra_c$. Error bars are the rms zonal velocities and correspond to the fluctuations associated with the thermal convection. The signal has been averaged over 400 seconds. Two minima are observed at s = 45 mm and 85 mm. The largest rms value observed around s = 100 mm are presumably associated with the presence of Rossby waves propagating in the external part of the shell.

and understood with a quasigeostrophic model. First, we give satisfying approximate solutions to the linear problem of convection onset in differential heating. Second, we reproduce many of the observed features of nonlinear convection, namely: chaotic convection as seen, for instance, by [*Cardin and Olson*, 1992], dual convection with thermal instabilities at both inner and outer boundaries, such as seen by [*Sumita and Olson*, 2000], mainly retrograde zonal circulations, measured by [*Sumita and Olson*, 2000; *Aubert et al.*, 2001]. The Doppler patterns of [*Aubert et al.*, 2001] are in remarkable agreement with the synthetics produced by the model. Experiments and simulations show that the shell contains both Rossby waves near the outer boundary, where the flow is weak, and much stronger vorticity structures near the inner boundary. These structures mix the background potential vorticity profile and thus create a retrograde zonal flow. In addition to the qualitative phenomena, quantitative aspects of the model, such as scaling relations for velocity in the nonlinear regime, have been successfully compared to experiments and theory.

[45] Some aspects, such as zonal flow in water experiments (Figure 13), remained difficult to compare with the numerical model. While [*Aubert et al.*, 2002] observed no or weak zonal flow in their water experiments, more recent experiments far from the onset of convection (typically $Ra/Ra_c > 40$) have shown detectable zonal flows, which are not understood. Neither the strength of the zonal wind nor the presence of two minima in its structure can be predicted by the quasigeostrophic numerical model.

[46] All other results give strong support to the use of a quasigeostrophic approximation for rotating convection modeling. However, one must keep in mind that it is a rough, and sometimes mathematically ill-posed approximation. To be completely rigorous it should be restricted to cases with weak boundary slope, as noted first by [*Busse*, 1970]. However Busse, and then [*Cardin and Olson*, 1994], and then the present study used it even when boundary slope is large. In our case we expected the approximation to fail near the outer boundary, where the spherical boundary slope becomes infinite. Comparing our results with experiments we have seen that the approach leads to a correct modeling throughout the shell. Indeed we use low Ekman numbers, and the lower the Ekman number is, the larger the boundary slope can be without breaking quasigeostrophy. The approach also neglects the rotation axis parallel transport of heat and subsequent thermal wind effects. For this reason it should be restricted to strongly forced nonlinear calculations, where the column-induced, axis-parallel circulation mixes heat in this direction. Moreover, the inclusion of the Ekman pumping contribution for some nonaxisymmetric modes in the numerical model may improve the agreement with experiments.

[47] The two-dimensional quasigeostrophic model for convection in a rotating spherical shell successfully describes both linear and nonlinear features of this phenomenon. This study provides quantitative tests of the model, especially for zonal flow where Ekman friction plays an important role.

[48] Reducing the dimensionality of velocity calculations is a very appealing way for solving dynamo problems in geophysically relevant conditions of turbulence, rapid rotation and high magnetic diffusion. The inclusion of quasigeostrophic velocity calculations in full dynamo mod-

els could represent a new possibility to achieve this fundamental goal.

Acknowledgments

[49] The authors would like to thank Daniel Brito, Henri-Claude Nataf and Dominique Jault for experimental help, discussions and suggestions. This work was supported by program *Intérieur de la Terre* of INSU/CNRS in France. J. A. also acknowledges support from *Marie Curie* fellowship program of the European Commission, under contract number HPMF-CT-2001-01364 during the finishing phase of this work. All the computations presented in this paper were performed at the *Service Commun de Calcul Intensif de l'Observatoire de Grenoble* (SCCI).

References

Aubert, J., D. Brito, H.-C. Nataf, P. Cardin, and J. P. Masson, A systematic experimental study of spherical shell convection in water and liquid gallium, *Phys. Earth Planet. Int.*, *128*, 51–74, 2001.

Aubert, J., S. Jung, and H. Swinney, Observations of zonal flow created by potential vorticity mixing in a rotating fluid, *Geophys. Res. Let.*, *29*(18), 1876, doi:10.1029/2002GL015422, 2002.

Brito, D., H.-C. Nataf, P. Cardin, J. Aubert, and J. Masson, Ultrasonic Doppler velocimetry in liquid gallium, *Exp. Fluids*, *31*, 653–663, 2001.

Busse, F. H., Thermal instabilities in rapidly rotating systems *J. Fluid. Mech.*, *44*, 441–460, 1970.

Busse, F. H., and C. R. Carrigan, Laboratory simulation of thermal convection in rotating planets and stars, *Science*, *191*, 81–83, 1976.

Cardin, P., and P. Olson, An experimental approach of thermochemical convection in the Earth's core, *Geophys. Res. Let.*, *19*, 1995–1998, 1992.

Cardin, P., and P. Olson, Chaotic thermal convection in a rapidly rotating spherical shell: Consequences for flow in the outer core, *Phys. Earth Planet. Int.*, *82*, 235–239, 1994.

Carrigan, C. R., and F. H. Busse, An experimental and theoretical investigation of the onset of convection in rotating spherical shells, *J. Fluid. Mech.*, *126*, 287–305, 1983.

Christensen, U. R., Zonal flow driven by deep convection in the major planets, *Geophys. Res. Let.*, *28*, 2553–2556, 2001.

Christensen, U. R., Zonal flow driven by strongly supercritical convection in rotating spherical shells, *J. Fluid. Mech.*, *470*, 115–133, 2002.

Christensen, U. R., et al., A numerical dynamo benchmark, *Phys. Earth Planet. Int.*, *128*, 25–34, 2001.

Glatzmaier, G. A., and P. Olson, Highly supercritical thermal convection in a rotating spherical shell: Centrifugal versus radial gravitiy, *Geophys. Astrophys. Fluid Dyn.*, *70*, 113–136, 1993.

Gubbins, D., and P. H. Roberts, Magnetohydrodynamics of the Earth's core, in *Geomagnetism*, edited by J. A. Jacobs, vol. 2, 1–183, Academic, San Diego, Calif., 1987.

Jones, C. A., A. M. Soward, and A. I. Mussa, The onset of thermal convection in a rapidly rotating sphere, *J. Fluid. Mech.*, *405*, 157–179, 2000.

Manneville, J., and P. Olson, Banded convection in rotating fluid spheres and the circulation of the Jovian atmosphere, *Icarus*, *122*, 242–250, 1996.

Nataf, H.-C., Dynamo and convection experiments, in *The Fluid Mechanics of Astrophysics and Geophysics*, edited by C. A. Jones, A. M. Soward, and K. Zhang, Taylor and Francis, Philadelphia, Pa., in press, 2003.

Pedlosky, J., *Geophysical Fluid Dynamics*, Springer-Verlag, New York, 1987.

Rhines, P. B., Waves and turbulence on a beta-plane, *J. Fluid Mech.*, *69*, 417–443, 1975.

Roberts, P. H., On the thermal instability of a self gravitating fluid sphere containing heat sources, *Philos. Trans. R. Soc. London Ser. A*, *263*, 93–117, 1968.

Sumita, I., and P. Olson, Laboratory experiments on high Rayleigh number thermal convection in a rapidly rotating hemispherical shell, *Phys. Earth Planet. Int.*, *117*, 153–170, 2000.

Zhang, K., and C. A. Jones, The influence of Ekman boundary layers on rotating convection, *Geophys. Astrophys. Fluid Dyn.*, *71*, 145–162, 1993.